



# Modeling Polarization Signals from Cloudy Brown Dwarfs Luhman 16 A and B in Three Dimensions

Sagnick Mukherjee<sup>1</sup> , Jonathan J. Fortney<sup>1</sup> , Rebecca Jensen-Clem<sup>1</sup> , Xianyu Tan<sup>2</sup> , Mark S. Marley<sup>3</sup> , and Natasha E. Batalha<sup>4</sup>

<sup>1</sup> Department of Astronomy and Astrophysics, University of California, Santa Cruz, CA 95064, USA; [samukher@ucsc.edu](mailto:samukher@ucsc.edu)

<sup>2</sup> Atmospheric, Oceanic and Planetary Physics, Department of Physics, University of Oxford, OX1 3PU, UK

<sup>3</sup> Lunar and Planetary Laboratory, The University of Arizona, Tucson, AZ 85721, USA

<sup>4</sup> NASA Ames Research Center, MS 245-3, Moffett Field, CA 94035, USA

Received 2021 June 23; revised 2021 October 4; accepted 2021 October 5; published 2021 December 15

## Abstract

The detection of disk-integrated polarization from Luhman 16 A and B in the  $H$  band, and subsequent modeling, has been interpreted in the framework of zonal cloud bands on these bodies. Recently, Tan and Showman investigated the 3D atmospheric circulation and cloud structures of brown dwarfs with general circulation models (GCMs), and their simulations yielded complex cloud distributions showing some aspects of zonal jets, but also complex vortices that cannot be captured by a simple model. Here we use these 3D GCMs specific to Luhman 16 A and B, along with the 3D Monte Carlo radiative transfer code ARTES, to calculate their polarization signals. We adopt the 3D temperature–pressure and cloud profiles from the GCMs as our input atmospheric structures. Our polarization calculations at  $1.6\ \mu\text{m}$  agree well with the measured degree of linear polarization from both Luhman 16 A and B. Our calculations reproduce the measured polarization for both objects with cloud particle sizes between  $0.5$  and  $1\ \mu\text{m}$  for Luhman 16 A and of  $5\ \mu\text{m}$  for Luhman 16 B. We find that the degree of linear polarization can vary on hour-long timescales over the course of a rotation period. We also show that models with azimuthally symmetric band-like cloud geometries, typically used for interpreting polarimetry observations of brown dwarfs, overpredict the polarization signal if the cloud patterns do not include complex vortices within these bands. This exploratory work shows that GCMs are promising for modeling and interpreting polarization signals of brown dwarfs.

*Unified Astronomy Thesaurus concepts:* [Brown dwarfs \(185\)](#); [Atmospheric clouds \(2180\)](#); [Atmospheric circulation \(112\)](#); [Polarimetry \(1278\)](#)

## 1. Introduction

Infrared spectroscopy of brown dwarfs has revealed a great deal of information about the thermal and chemical structure of their atmospheres (Kirkpatrick 2005). These observations also have long suggested the presence of clouds in their atmospheres (Helling & Casewell 2014; Marley & Robinson 2015). However, cloud properties like altitudes, vertical extent, and typical particle sizes are difficult to interpret from thermal spectroscopy or photometry. Moreover, time-series photometry and spectroscopy have often found these objects to be variable (Buenzli et al. 2015; Apai et al. 2021; Miles-Páez et al. 2015; Eriksson et al. 2019; Miles-Páez et al. 2017; Artigau et al. 2009; Radigan et al. 2012; Girardin et al. 2013; Radigan et al. 2014; Vos et al. 2019) suggesting nonuniform cloud coverage, which further complicates the interpretation of these observations.

Additional observational and theoretical tools could potentially break important new ground in our understanding of substellar atmospheres. One such avenue is polarization. Thermal emission arising from substellar atmospheres may become partially linearly polarized due to scattering from cloud/dust particles present in the atmosphere. Rayleigh scattering from gas molecules in the atmosphere can also give rise to significant polarization in optical wavelengths. However, this gets suppressed in the near-infrared due to the sharp decline of Rayleigh scattering with increasing wavelength (Marley & Sengupta 2011). Therefore thermal polarized emission in near-infrared wavelengths mainly arises from the

Mie particle scattering of thermal photons by cloud particles that are present.

However, the observable disk-integrated polarization from perfectly spherical and uniformly cloudy objects cancels out to zero even though the local polarized surface brightness of the object might be nonzero. A detectable nonzero disk-integrated polarization can still arise if this symmetry is broken either by rotationally induced oblateness of the object or by nonuniformity of the cloud cover (Sengupta & Krishan 2001; Sengupta & Marley 2010; de Kok et al. 2011; Marley & Sengupta 2011). For self-luminous gas giant planets, cousins of brown dwarfs, the presence of circumplanetary disks (Stolker et al. 2017) or transiting exomoons (Sengupta & Marley 2016) can also break this symmetry for spherical objects and produce net disk-integrated polarized flux.

The sensitivity of the disk-integrated polarization signal to rotationally induced oblateness, the inclination of the spin axis of the object, gravity, effective temperature, and cloud particle sizes has been theoretically studied in detail for uniformly cloudy exoplanets and brown dwarfs (Sengupta & Krishan 2001; Sengupta & Marley 2010; Marley & Sengupta 2011; de Kok et al. 2011; Sanghavi & Shporer 2018; Sanghavi & West 2019; Sanghavi et al. 2021). Model calculations of disk-integrated polarization signals arising from nonuniform cloud coverage on exoplanets and brown dwarfs have been performed by de Kok et al. (2011) and Stolker et al. (2017), yielding polarization signal predictions typically  $\geq 0.1\%$  in near-infrared wavelengths. At that level, near-infrared polarimetric and spectropolarimetric observations of

brown dwarfs can provide us with that additional diagnostic window into the nature of clouds in these atmospheres.

A number of observations of polarized emission from brown dwarfs have been published as well over the past two decades (Ménard et al. 2002; Zapatero Osorio et al. 2005, 2011; Goldman et al. 2009; Tata et al. 2009; Miles-Páez et al. 2013; Manjavacas et al. 2017; Millar-Blanchaer et al. 2020). Recently, upper limits on polarized thermal emission have been determined for a large sample (23) of exoplanets and brown dwarf companions (Millar-Blanchaer et al. 2015; Jensen-Clem et al. 2016; van Holstein et al. 2017; Jensen-Clem et al. 2020; van Holstein et al. 2021) using the Gemini Planet Imager (Macintosh et al. 2014) and the Spectro-polarimetric High-contrast Exoplanet Research instrument (Beuzit et al. 2019). Van Holstein et al. (2021) found that polarized thermal emission measurements from DH Tau B and GSC 6214-210 B hint at the presence of circumsubstellar disks. Time-domain photometric observations of some brown dwarf objects detected in polarized emission have additionally revealed significant variability in thermal flux (Buenzli et al. 2015; Apai et al. 2021) and polarized flux (Miles-Páez et al. 2015). This suggests not only the presence of clouds in these objects but might also hint at nonuniformity in the cloud cover. However, no significant statistical correlation between the detection of polarized thermal emission and the presence of variability has been found yet. Nearly 40% of brown dwarfs near the L–T transition are found to be strongly variable (Eriksson et al. 2019), which suggests that these objects commonly have patchy cloud coverage, as has been suggested on theoretical grounds (Ackerman & Marley 2001; Burgasser et al. 2002).

Our nearest binary brown dwarf pair Luhman 16 A and B (Luhman 2013) is especially interesting in this context, as Luhman 16 A has a spectral type of L7.5 and Luhman 16 B is a T0.5 dwarf (Burgasser et al. 2013; Kniazev et al. 2013). As both of these objects are near the L–T transition, there is a good chance that they have nonuniform cloud cover (Saumon & Marley 2008). Two-dimensional Doppler mapping of Luhman 16 B by Crossfield et al. (2014) found bright and dark regions across the globe, which are indicative of cloud nonuniformity. Buenzli et al. (2015) have shown that the thermal spectra of both objects can be adequately fit with the superposition of two models with different cloud properties and coverage fractions. Multiple time-domain photometric studies have also found both components to be variable (Buenzli et al. 2015; Apai et al. 2021) further hinting at patchy cloud coverage.

Millar-Blanchaer et al. (2020) recently made the first detection of polarized thermal emission from each of the components of the binary system Luhman 16 A and B. The *H*-band degree of linear polarization for Luhman 16 A and Luhman 16 B was measured to be 0.031% and 0.010%, respectively, with a precision of 0.004%, thus providing  $7.5\sigma$  and  $2.5\sigma$  detections. The angle of the polarization vector was also measured for both objects. Atmospheric modeling by Millar-Blanchaer et al. (2020) of the disk-integrated polarization signal showed that the measured polarization signal from Luhman 16 B can arise from a uniformly cloudy oblate object or from a nonuniformly cloudy configuration. However, the polarization signal from Luhman 16 A could only be explained by nonuniform cloud coverage, for example by multiple bands of relatively cloudy regions on the object (Millar-Blanchaer et al. 2020). This detection and the subsequent analysis emphasize that nonuniformity in cloud cover should be

considered while interpreting polarimetric (or even nonpolarimetric) observations of brown dwarfs near the L–T transition.

An essential tool to understanding 3D phenomena in substellar atmospheres is general circulation models (GCMs). Such models couple fluid dynamics in 3D with radiative transfer, to understand energy transport throughout an atmosphere (Showman et al. 2020). A realization of the 3D temperature and wind structure, when coupled with a treatment of cloud formation, yields physically motivated predictions of substellar atmospheres. These GCMs provide the idealized basic structure of the atmosphere, which can be post-processed with robust radiative transfer calculation codes like ARTES (Stolker et al. 2017) enabling direct comparisons with polarimetric observations.

Tan & Showman (2021a, 2021b) have recently developed 3D circulation models for brown dwarfs that include a variety of cloud phenomena, like condensation of clouds and cloud radiative feedback, in order to simulate the global circulation and cloud patterns of rotating brown dwarfs. This gives us the opportunity to model the polarization signals emitted from these physically motivated, inherently 3D and nonuniform cloud distributions, to test if they can match the observations of Luhman 16 A and B. In this work, for the first time we use 3D circulation models and post-process them with the vector Monte Carlo radiative transfer code ARTES to interpret the polarimetric data, focusing on the observations of Luhman 16 A and Luhman 16 B from Millar-Blanchaer et al. (2020). Despite the low statistical significance of the detection of the polarization of Luhman 16 B, this object is of high interest to the astronomical community due to its proximity and significant variability, and we therefore consider it worthwhile to carry this modeling exercise on both A and B components. We specifically aim to explore and answer the following:

1. Can GCMs with appropriate parameters for Luhman 16 A and Luhman 16 B be post-processed with a radiative transfer code like ARTES to match their observed polarization measurements?
2. Do these GCMs also match the observed photometric variability in Luhman 16 A and B?
3. Are the calculated polarization signals from circulation models of brown dwarfs sensitive to the spin axis inclination relative to our line of sight of the objects?
4. How sensitive is the disk-integrated polarization signal arising from GCMs of brown dwarfs to the typical cloud particle sizes?
5. Are cloud band models an adequate approximation when calculating polarization signals from objects that have nonuniform cloud covers including vortices of cloudy and clear regions?

We describe our modeling of the atmospheric circulation, cloud structures, and polarized emission in Section 2, present the results in Section 3, discuss our findings in Section 4, and provide a summary and conclusions in Section 5.

## 2. Modeling Substellar Atmospheres

### 2.1. GCMs of Brown Dwarfs

We use the GCMs described and used in Tan & Showman (2021a, 2021b) to simulate the 3D temperature and cloud structure for brown dwarfs Luhman 16 A and Luhman 16 B. The circulation models solve the fluid equations governing the

**Table 1**  
The Brown Dwarf Parameters and Values Used to Model the 3D Circulation Patterns for Luhman 16 A and Luhman 16 B

Parameter	Model (16 A)	Model (16 B)	Measurement (16 A)	Measurement (16 B)
Rotation Period	7 hr	5 hr	6.94 hr <sup>a</sup>	5.28 hr $\pm$ 22% <sup>a, b</sup>
Log( <i>g</i> )	4.5	5	4.5 <sup>c</sup>	4.5–5 <sup>c</sup>
Radius	$7 \times 10^7$ m	$6.3 \times 10^7$ m	$0.95 R_J^c$	$0.8\text{--}0.93 R_J^c$
$N_c$	$1 \times 10^9 \text{ kg}^{-1}$	$1 \times 10^8 \text{ kg}^{-1}$	...	...
Cloud Material Density	$3.19 \text{ g cm}^{-3}$	$3.19 \text{ g cm}^{-3}$	...	...
Temperature (100 bars)	4300 K	3500 K	...	...

**Notes.** The measured values of these parameters are also shown except for those parameters that have not yet been measured but have been assumed in our modeling.

<sup>a</sup> Apai et al. (2021).

<sup>b</sup> Relative period range as reported in Apai et al. (2021).

<sup>c</sup> Buenzli et al. (2015).

horizontal momentum, mass continuity, hydrostatic balance, and energy transport of the substellar atmosphere in a rotating frame of reference. Two tracer equations are solved for the dynamics of the vapor and cloud components of the atmosphere. The radiative transfer for thermally emitted photons is computed using the gray atmosphere approximation in these models. The detailed physics and the governing equations of the GCM are fully described in Tan & Showman (2021b). We use the temperature structures and cloud distributions from these GCMs for calculating the disk-integrated polarized flux from Luhman 16 A and Luhman 16 B. Table 1 summarizes the physical input parameters used for simulating the circulation patterns for both objects.

$N_c$  in Table 1 denotes the cloud particle number per dry air mass for each object. The cloud material density used in the simulations corresponds to that of enstatite ( $\text{MgSiO}_3$ ).  $N_c$  controls the mean cloud particle sizes in each radial bin in our GCM according to Equation (1) (see below) and the value of  $N_c$  for each object shown in Table 1 is such that Luhman 16 A and B have typically  $1 \mu\text{m}$  and  $5 \mu\text{m}$  sized cloud particles, respectively, near the base of their cloud decks. We explore the effect of having different-sized cloud particles on the disk-integrated polarization signal from these objects in Section 3.

The GCMs for Luhman 16 A use  $60 \times 190 \times 384$  grid cells corresponding to the  $r$ ,  $\theta$ , and  $\phi$  variables, respectively, where  $r$  is the radial dimension,  $\theta$  is the polar dimension, and  $\phi$  is the azimuthal dimension. Models for Luhman 16 B use a  $60 \times 254 \times 512$  grid. The higher angular resolution used for Luhman 16 B is due to the fact that it is a faster rotator, which requires following the dynamics on smaller length scales. The GCM for both objects evolves somewhat over time but here we use a time snapshot of the model after it reaches a steady state. We now describe the modeled thermal and cloud structures from the GCM setups in Sections 2.1.1 and 2.1.2.

### 2.1.1. The 3D Temperature–Pressure Structure

The temperature patterns at a pressure level of  $\sim 0.23$  bars arising across the globe for both brown dwarfs are shown in Figure 1. This is a representative pressure chosen to be within the enstatite cloud for both objects. The central band of comparatively hotter regions is very evident for Luhman 16 A whereas for Luhman 16 B such a distinct central hot band is missing at this pressure level. As Luhman 16 A has been assumed to be a slower rotator than Luhman 16 B, the

horizontal length scales of various vortices and features for Luhman 16 A are larger than those for Luhman 16 B. The Rossby deformation radius is inversely proportional to the Coriolis parameter ( $f$ ) and guides the typical length scales of vortices (Tan & Showman 2021b) and as a result this difference in length scales of vortices arises in our models.

The longitudinally averaged temperature–pressure ( $T$ - $P$ ) profile for both Luhman 16 A and B is shown in Figure 2 with colored solid lines from the equatorial regions to the polar regions. The  $T$ - $P$  profiles in the deep interior ( $\geq 10$  bars) all converge to the same adiabat due to the onset of convection at such high pressures in both objects. For Luhman 16 A, the equatorial regions are hotter than the polar regions at lower pressures ( $\leq 1$  bar). This behavior can be attributed to cloud radiative feedback. The equatorial regions for both objects are relatively cloudier than the polar regions as can be seen in Figure 1, lower left panel. Higher cloud opacities scatter and absorb more thermal flux and as a result heat up the atmospheric columns more significantly in the equatorial regions than in the polar regions.

The thermal structure of Luhman 16 B is more homogeneous compared to that of Luhman 16 A as can be seen in both Figures 1 and 2. This is related to the cloud optical depth variation for both objects across the globe. Cloud particle sizes show higher variations across the globe in Luhman 16 A than in Luhman 16 B, which can be seen both in the Figure 1 lower panels and in Figure 2 (dotted lines). This causes the cloud radiative feedback on Luhman 16 B to be more homogeneous than that on Luhman 16 A leading to a comparatively homogeneous thermal structure in Luhman 16 B relative to Luhman 16 A.

### 2.1.2. The 3D Cloud Structure

The GCMs treat the condensation and particle formation of  $\text{MgSiO}_3$  (enstatite) for both objects.  $\text{MgSiO}_3$  is a dominant cloud species for objects with effective temperatures for Luhman 16 A and B and has been chosen here as a representative silicate. However, other species like Fe clouds might also be important sources of scattering in the atmosphere but they are not expected to critically affect the cloud circulation patterns as long as the cloud opacities are greater than the gas opacities. We discuss this further in Section 4.

The condensing species in the GCM, enstatite, does not exist in the vapor phase. But it condenses through a chemical



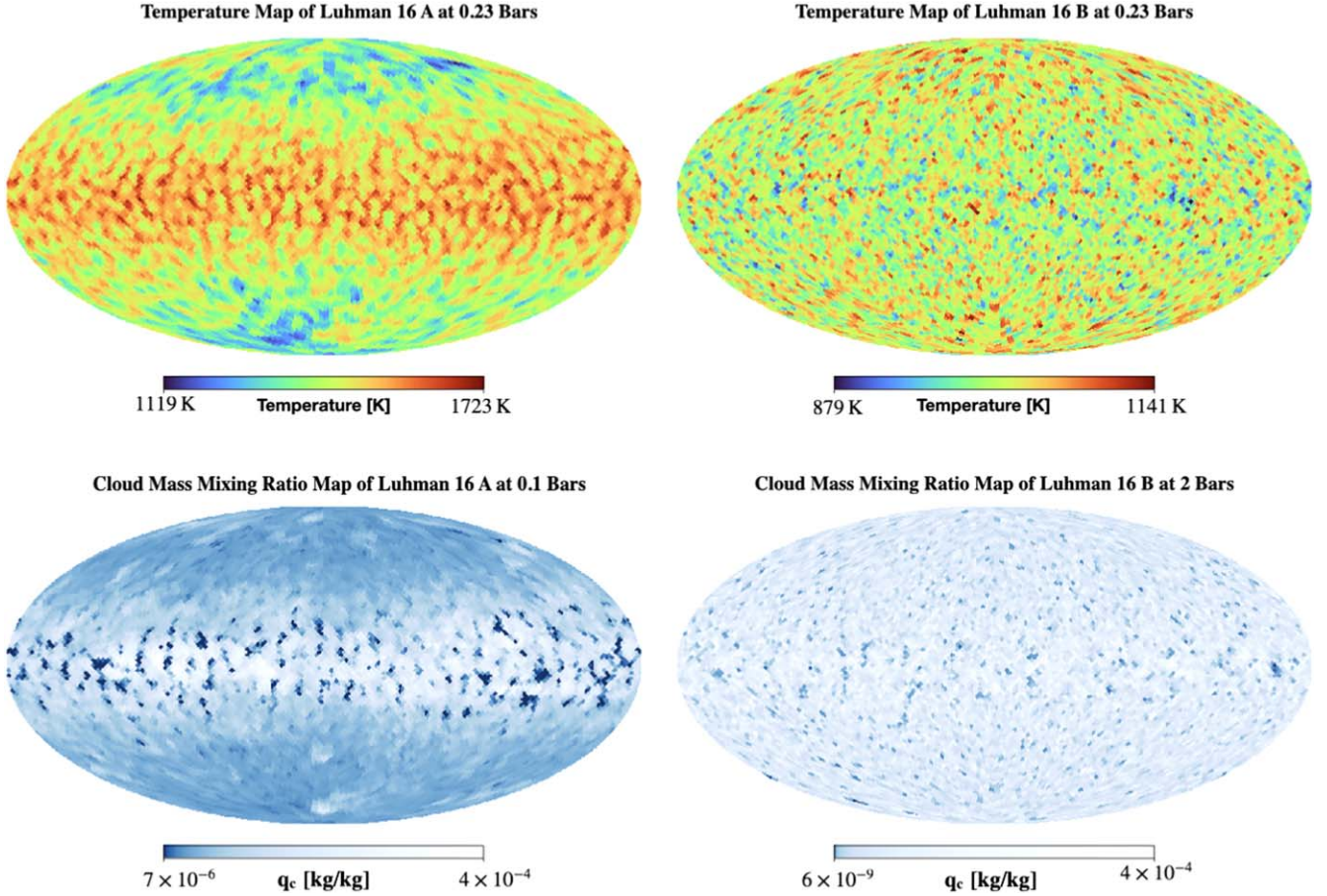


**Figure 1.** The top panel shows the global temperature pattern from the GCM runs at a pressure of 0.23 bars for Luhman 16 A (top left panel) and Luhman 16 B (top right panel). The bottom panels show the cloud mass mixing ratio ( $q_c$ ) at a pressure of 0.1 bars for Luhman 16 A (bottom left panel) and at a pressure level of 2 bars for Luhman 16 B (bottom right panel). Main point: The equator is hotter and cloudier than the poles for Luhman 16 A; furthermore, the sizes of vortices in the Luhman 16 A and B models are different due to these objects’ different rotation rates.

pathway involving a reaction between gaseous magnesium, water vapor, and SiO (Visscher et al. 2010). This reaction can only occur across a pressure–temperature curve which we refer to as the phase boundary curve for enstatite. This phase boundary curve for enstatite has been treated similarly to a condensation curve for species that condense directly from their vapor phase (like  $\text{H}_2\text{O}$ ) in our GCM. The gaseous vapor phase Mg in our GCM condenses to enstatite cloud particles when the local mass mixing ratio of the condensible vapor is higher than the local saturation vapor mixing ratio ( $q_s$ ). On the other hand, when the local cloud mixing ratio ( $q_c$ ) exceeds the saturation vapor mixing ratio ( $q_s$ ), it evaporates and turns back to vapor. The local saturation vapor mixing ratio  $q_s$  is determined by the temperature–pressure-dependent phase boundary curve of enstatite given by Visscher et al. (2010) using solar abundance and is shown in Figure 2 with black solid lines. The detailed implementation for condensates is the same as that in Tan & Showman (2019).

In Figure 1 the bottom left panel shows the  $q_c$  at a 0.1 bar pressure for our models of Luhman 16 A and the bottom right panel shows the  $q_c$  at a 2 bar pressure for our models of Luhman 16 B. The pressure levels are chosen here for highlighting the equator-to-pole trends of the cloud structure in the GCMs near the base of the cloud decks for each object. The pressure dependence of the clouds and their equator-to-pole trends can be seen in Figure 2. The sizes of cloud vortices

decrease from the equator toward the pole for both objects due to the variation of the Coriolis parameter  $f$  with  $\phi$  across the globe. Also, Luhman 16 A has larger cloud patterns than Luhman 16 B due to the difference in their rotation periods, as has been discussed earlier in the context of temperature patterns.

We determine the mean cloud particle size of each layer using the following equation (Tan & Showman 2021b):

$$r_c = \left( \frac{3q_c}{4\pi N_c \rho_c} \right)^{1/3} \quad (1)$$

where  $q_c$  is the cloud mass mixing ratio and  $\rho_c$  is the material density of our cloud species, which has been specified in Table 1.

The longitudinally averaged cloud particle sizes are shown for different latitudes from the equator to the pole for Luhman 16 A (left) and Luhman 16 B (right) in Figure 2 with dotted lines. As has been noted in Tan & Showman (2021a), faster rotation leads to vertically thinner cloud decks for Luhman 16 B compared to Luhman 16 A. The typical cloud particle size for the Luhman 16 A model is  $\sim 1 \mu\text{m}$  whereas that for Luhman 16 B is  $\sim 5 \mu\text{m}$ . This is analogous to a low value of  $f_{\text{sed}}$ , vertically thicker clouds with smaller particles (Luhman 16 A model), and a high value of  $f_{\text{sed}}$ , vertically thinner clouds with larger particles (Luhman 16 B model), within the framework of the Ackerman & Marley (2001) cloud model. Buenzli et al.

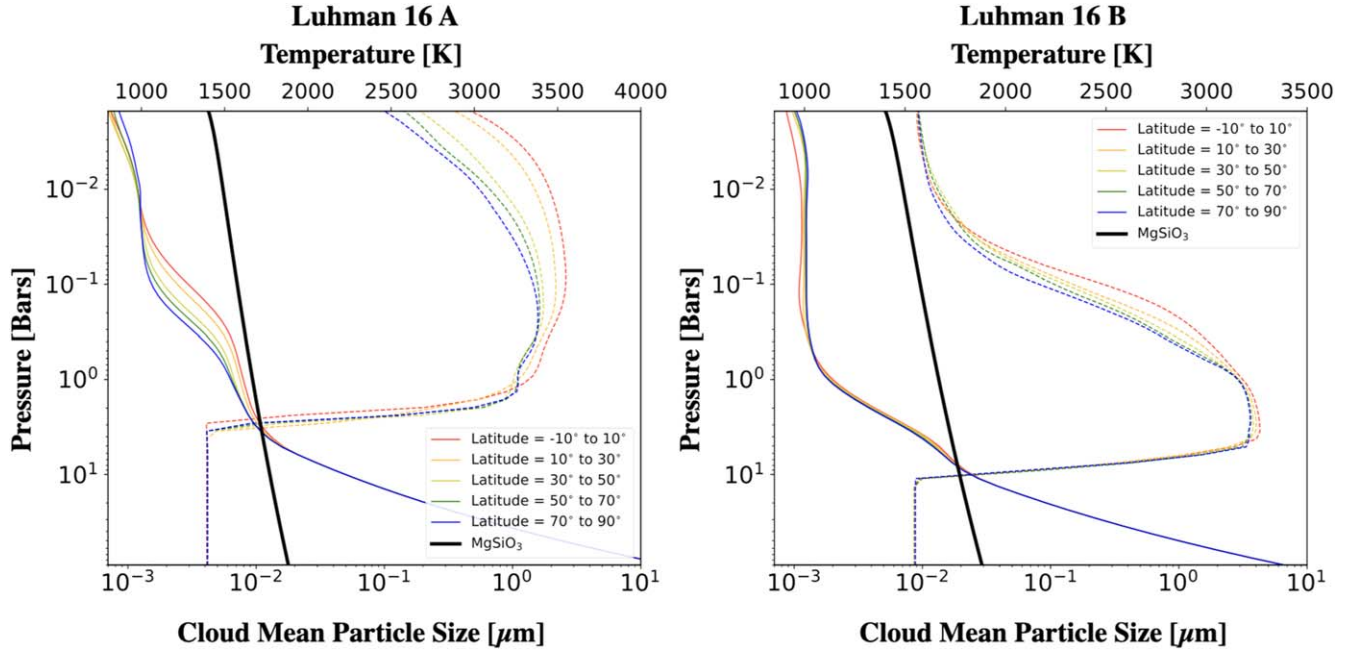


**Figure 2.** The left panel shows the longitudinally averaged  $T$ - $P$  profiles for Luhman 16 A with solid lines. Various colored lines depict the average  $T$ - $P$  profiles of the latitudinal bands each with an angular width of  $20^\circ$  from the equator (red) to the pole (blue). The black solid line shows the phase boundary curve for enstatite from Visscher et al. (2010) assuming solar abundance. The dotted colored lines depict the longitudinally averaged cloud particle sizes in micrometers from the equator to the poles. The right panel depicts the same for Luhman 16 B.

(2015) found that spectroscopic variability data for the A component is best fit with an  $f_{\text{sed}} = 2$  model whereas B component data could be best fit with a superposition of a hotter model with thinner clouds of  $f_{\text{sed}} = 3$  and a colder model with thicker clouds of  $f_{\text{sed}} = 1$ . In addition, our GCM finds that cloud thickness decreases toward the pole from the equator due to the variation of the Coriolis parameter  $f$  with latitude. Table 1 shows the number of cloud particles per dry air mass ( $N_c$ ), which has been assumed to be larger for Luhman 16 A than for Luhman 16 B as the former is classified as an L dwarf and the latter a T dwarf (Burgasser et al. 2013; Kniazev et al. 2013). This results in larger typical cloud particle sizes for Luhman 16 B than for the Luhman 16 A model.

## 2.2. Radiative Transfer with ARTES

We use the publicly available 3D Monte Carlo radiative transfer code ARTES<sup>5</sup> (Stolker et al. 2017) for post-processing the 3D atmospheric structure calculated from the GCMs. The radiative transfer formalism of ARTES involves the emission of photon packages from each grid cell of the 3D atmosphere grid. These photons are stochastically absorbed or scattered as they travel through the atmosphere ultimately hitting the detector once they escape. The initial emission direction of the photons is sampled from a probability distribution function that is biased toward emitting photons in the radially outward direction. The probability distribution function (Stolker et al. 2017)  $p(\zeta)$  is

$$p(\zeta) = \frac{\sqrt{1 - \epsilon^2}}{\pi(1 + \epsilon \cos \zeta)} \quad (2)$$

where  $\zeta$  is the emission direction and varies between 0 (radially downward) and  $\pi$  rad (radially outward) and  $\epsilon$  is the asymmetry

parameter for the emission, which varies between 0 and 1. A higher asymmetry parameter ( $\epsilon$ ) leads to a larger number of photons emitted initially toward the radially outward direction. Since we are mainly concerned about outgoing thermal emission from the atmosphere, we use  $\epsilon = 0.8$  for all our radiative transfer calculations. This is a valid approximation because scattering events that can change the direction of photons emitted to radially downward directions to radially upward directions are possible but unlikely.

Each photon has a Stokes vector of the form

$$S = \begin{pmatrix} I \\ Q \\ U \\ V \end{pmatrix} \quad (3)$$

where  $\pi I$  is the thermal flux. The degree of linear polarization ( $P$ ) and the angle of the polarization vector ( $\chi$ ) for each photon are given by

$$P = \frac{\sqrt{Q^2 + U^2}}{I} \quad (4)$$

$$\chi = \frac{1}{2} \arctan\left(\frac{U}{Q}\right). \quad (5)$$

Each scattering event leads to the rotation of the Stokes vector for each photon using a matrix multiplication operation involving the scattering matrix and the rotation matrix depending on the scattering direction of the photon. This operation is described in detail in Stolker et al. (2017). The final Stokes parameters of the escaped photons are then projected on the detector. The additive nature of the Stokes vectors allows the projected Stokes vectors to be simply added to calculate the disk-integrated Stokes vector of the object. This disk-integrated Stokes vector is then used to calculate the disk-

<sup>5</sup> <https://github.com/tomasstolker/ARTES>



integrated flux, the degree of linear polarization, and the angle of linear polarization using Equations (4) and (5).

We use  $1 \times 10^{11}$  photons for all of our calculations to maintain sufficient accuracy ( $\leq 10\%$  Monte Carlo error) in the calculated thermal and polarized flux. For computational purposes, we regrid the GCMs into  $60 \times 85 \times 171$  grid cells ( $r \times \theta \times \phi$ ) for both Luhman 16 A and B. We assume a detector with  $100 \times 100$  pixels for our calculations. We ensure that our resolution is high enough to preserve the overall circulation patterns of the original GCM runs described in Section 2.1 for both bodies.

### 2.3. Opacities and Scattering Matrices

We use the molecular and continuum opacity database available in the open-source code PICASO (Batalha et al. 2019, 2020) for our calculations. Molecular opacities from  $\text{H}_2\text{O}$  (Barber et al. 2006; Tennyson & Yurchenko 2018),  $\text{CH}_4$  (Yurchenko et al. 2013; Yurchenko & Tennyson 2014),  $\text{NH}_3$  (Yurchenko et al. 2011),  $\text{CO}$  (Li et al. 2015),  $\text{PH}_3$  (Sousa-Silva et al. 2014),  $\text{H}_2\text{S}$  (Azzam et al. 2016),  $\text{CO}_2$  (Huang et al. 2014),  $\text{Na}$  and  $\text{K}$  (Ryabchikova et al. 2015),  $\text{TiO}$  (Schwenke 1998), and  $\text{VO}$  (McKemmish et al. 2016) are included. Collision-induced absorption opacities from  $\text{H}_2\text{--H}_2$  (Abel et al. 2011),  $\text{H}_2\text{--He}$ ,  $\text{H}_2\text{--N}_2$ ,  $\text{H}_2\text{--H}$ ,  $\text{H}_2\text{--CH}_4$ ,  $\text{H}\text{--electron bound-free}$ ,  $\text{H}\text{--electron free-free}$ , and  $\text{H}_2\text{--electron interactions}$  are also included. We use the average  $T$ - $P$  profile of the entire globe to calculate the molecular abundances and atmospheric opacities of these molecules assuming thermochemical equilibrium with solar values for  $\text{C/O}$  ratio and metallicity. For computational efficiency, we neglect the variation of the equilibrium molecular abundances due to the changing  $T$ - $P$  profile across the radial columns of the atmosphere. As we focus on polarization at a particular wavelength, rather than precision spectroscopy across a broad wavelength range, this simplification is warranted for this particular work. We discuss this further in Section 4.

We assume that the cloud particle sizes follow a gamma distribution (Hansen 1971; Stolker et al. 2017) although the GCM runs include only single-sized particles. The cloud particle size distribution is given by

$$n(r) = Cr^{(1-3v_{\text{eff}})/v_{\text{eff}}} e^{-r/v_{\text{eff}} r_{\text{eff}}} \quad (6)$$

where  $r_{\text{eff}}$ ,  $v_{\text{eff}}$ , and  $C$  are the effective radius, effective variance, and normalization constant, respectively. The Figure 3 top panels show the particle size distribution for various combinations of  $r_{\text{eff}}$  and  $v_{\text{eff}}$ . The solid lines show the particle size distributions when  $v_{\text{eff}} = 0.05$  and  $r_{\text{eff}}$  is 0.1 ( $\mu\text{m}$ ), 1 (red), and 10 (green)  $\mu\text{m}$ . The dotted lines show the distributions when  $v_{\text{eff}} = 0.1$  and  $r_{\text{eff}}$  is 0.1 (blue), 1 (red), and 10 (green)  $\mu\text{m}$ . Other cloud models like that of Ackerman & Marley (2001) assume a lognormal distribution of particle sizes. The gamma particle size distributions differ from the lognormal distribution because of its asymmetry. It represents clouds where the probability density is higher for larger particles near  $r_{\text{eff}}$  with a broader distribution of smaller particles.

For each  $(r, \theta, \phi)$  grid point we assume  $r_{\text{eff}}$  to be the cloud particle radius from Equation (1) and  $v_{\text{eff}}$  to be 0.05. We then calculate the particle size distribution in 80 radial bins and calculate the absorption opacity, scattering opacity, and scattering matrix elements in each of these radial bins using

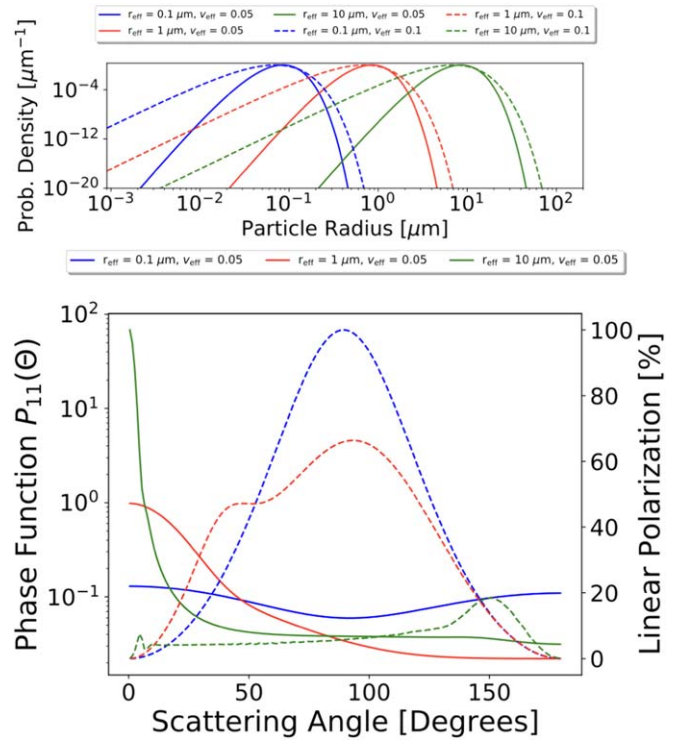


**Figure 3.** The top panel shows the cloud particle size distributions for different values of effective radius ( $r_{\text{eff}}$ ) and effective variance  $v_{\text{eff}}$ . The solid lines depict the particle size distributions with  $v_{\text{eff}} = 0.05$  and  $r_{\text{eff}}$  of 0.1  $\mu\text{m}$  (blue solid line), 1  $\mu\text{m}$  (red solid line), and 10  $\mu\text{m}$  (green solid line). The dashed lines show wider particle size distributions with  $v_{\text{eff}} = 0.1$  and  $r_{\text{eff}}$  of 0.1  $\mu\text{m}$  (blue dashed line), 1  $\mu\text{m}$  (red dashed line), and 10  $\mu\text{m}$  (green dashed line). The bottom panel's left vertical axis corresponds to the phase function ( $P_{11}(\Theta)$ ). The solid lines show  $P_{11}(\Theta)$  calculated from the particle size distributions shown in the top panel with the same colors. The percentage of linear polarization as a function of the scattering angle is shown with dashed lines for each of the particle distributions (right vertical axis). Main point: Gas and clouds scatter infrared light very differently and single-scattering polarizations are very sensitive to particle sizes.

Mie particle scattering theory. We obtain the complex refractive indices of amorphous magnesium silicates similar to enstatite in composition from Scott & Duley (1996) and use them for all our cloud opacity and scattering matrix calculations. These opacities and matrix elements are then integrated over the size distribution to obtain the total cloud opacities and scattering matrix elements for that grid point. This calculation is done using the Mie calculation module in ARTES (Stolker et al. 2017). The scattering matrices for the gas and cloud particles are calculated using the following form (Hansen & Travis 1974; Stolker et al. 2017):

$$S = \begin{pmatrix} P_{11}(\Theta) & P_{12}(\Theta) & 0 & 0 \\ P_{12}(\Theta) & P_{22}(\Theta) & 0 & 0 \\ 0 & 0 & P_{33}(\Theta) & P_{34}(\Theta) \\ 0 & 0 & -P_{34}(\Theta) & P_{44}(\Theta) \end{pmatrix} \quad (7)$$

where  $\Theta$  is the angle between the directions of the incident and scattered light. The  $P_{11}(\Theta)$  component represents the phase function of the scattering when it is normalized appropriately such that  $\frac{1}{2\pi} \int_0^\pi P_{11}(\Theta) \sin(\Theta) d\Theta = 1$ . As the gas particle sizes are much smaller than infrared wavelengths, this matrix is calculated in the Rayleigh scattering regime for the gas

particles, where

$$\begin{aligned} P_{11}(\Theta) &= \frac{3\pi}{4}(1 + \cos^2 \Theta) & P_{12}(\Theta) &= \frac{3\pi}{4}(1 - \cos^2 \Theta) \\ P_{22}(\Theta) &= P_{11}(\Theta) & P_{33}(\Theta) &= \frac{3\pi}{4}(2 \cos \Theta) \\ P_{44}(\Theta) &= P_{33}(\Theta) & P_{34}(\Theta) &= 0. \end{aligned}$$

This Rayleigh scattering matrix represents a situation where the incident wave front is scattered symmetrically in the forward and backward directions. Since the cloud particles scatter infrared photons in the Mie particle scattering regime, the cloud scattering matrix is calculated using the full Mie theory with the Mie calculation module in ARTES. The Mie scattering matrix for micron-sized cloud particles produces asymmetrically scattered wave fronts. This is shown in Figure 3, bottom panel. The solid lines show the Mie particle scattering phase function ( $P_{11}(\Theta)$ ) for a wavelength of  $1.6 \mu\text{m}$  for the three particle size distributions shown in the top panel with the solid lines corresponding to  $v_{\text{eff}} = 0.05$  and  $r_{\text{eff}} = 0.1$  (blue), 1 (red), and 10 (green)  $\mu\text{m}$ . The dotted lines show the polarization percentage from a single-scattering event as a function of scattering angle. The phase function in solid blue shows that particles scatter light symmetrically in the forward and the backward direction with less light scattered at an angle of  $90^\circ$  when  $r_{\text{eff}}$  is  $\sim 0.1 \mu\text{m}$ . The polarization percentage for  $\sim 0.1 \mu\text{m}$  particles peaks at a scattering angle of  $90^\circ$ , which is typical Rayleigh scattering behavior. Particle size distributions with typically larger particles like  $r_{\text{eff}}$  of 1 or 10  $\mu\text{m}$  show much higher amounts of forward scattering compared to backward scattering. With increasing particle sizes, the degree of linear polarization also departs from Rayleigh regime behavior.

### 3. Results

#### 3.1. Luhman 16 A

We first calculate the thermal flux and linear polarization percentage for Luhman 16 A at  $1.6 \mu\text{m}$ . This choice of wavelength is motivated by the recent measurement of the polarization of Luhman 16 A in the  $H$  band by Millar-Blanchaer et al. (2020). The measured polarization is  $0.031\% \pm 0.004\%$ . For Luhman 16 A, we assume a rotation period of 7 hr (Apai et al. 2021) and a rotationally induced oblateness of 0.003, which is expected of a Luhman 16 A–like body with a rotational period of 7–8 hr (Millar-Blanchaer et al. 2020). We assume an inclination of  $28^\circ$  for our initial calculation ( $0^\circ$  is equator-on hereafter). This is motivated by the recent measurements of inclination of  $\leq 28^\circ$  for Luhman 16 A by Apai et al. (2021). We explore other inclinations closer to the equator-on view as well and describe the results from them. We calculate the polarization and flux signals from our Luhman 16 A GCM every 52.5 minutes as the object rotates for a total of one rotation period. This interval is chosen such that we repeat our calculation after every  $45^\circ$  rotation of the object along the spin axis. The Figure 4 left panels show the surface brightness map of Luhman 16 A, the thermal flux variability, the linear polarization percentage variability, and the angle of polarization variability from top to bottom.

The surface brightness map for Luhman 16 A shows the thermal flux at  $1.6 \mu\text{m}$  from each pixel at a single time snapshot as the object is rotating. The central relatively cloudy band is readily visible to be slightly off-center in the image due to the assumed  $28^\circ$  inclination of the object. The cloudy regions emit

less thermal flux and appear darker because they scatter/absorb more light compared to the clear regions. The flux variability of the object for one complete rotational period is shown with a yellow solid line. The peak-to-peak variability of the thermal flux is about 5%, which mainly arises from the varying cloud patterns across the globe in our GCM. Buenzli et al. (2015) measured a 4% peak-to-peak variability of Luhman 16 A within the  $0.8\text{--}1.15 \mu\text{m}$  wavelength range. Our results do not reproduce the Buenzli et al. (2015) measurement within a  $1\sigma$  uncertainty. Our calculated flux variability is also larger than the measurements of Apai et al. (2021), who inferred a typical peak-to-peak variability amplitude of 2.2% for Luhman 16 A using TESS light curves of the system in the wavelength range of  $0.6\text{--}1.0 \mu\text{m}$ . But these differences can be due to the difference between the wavelength of our calculations ( $1.6 \mu\text{m}$ ) and the observed wavelengths as the variability amplitude can vary strongly with wavelength (Buenzli et al. 2015). Biller et al. (2013) measured the  $H$ -band peak-to-peak amplitude for the unresolved Luhman 16 binary to be  $\sim 4\%$ . However, the  $H$ -band amplitude of the Luhman 16 A component alone remained below the detection limits of their observations. Differences in variability amplitudes can also arise if our circulation model does not capture the “true” cloud distribution and/or particle sizes in these objects.

The time-varying modeled polarization signal is shown with a red solid line and is compared to the measured time-averaged signal in black for Luhman 16 A (Millar-Blanchaer et al. 2020). The uncertainty in the measured polarization is shown with a black shaded region. The modeled polarization signal agrees well with the time-averaged measurement. But importantly, the degree of polarization also shows significant variation within 0.03% to 0.045% within one rotational period.

Variability of linear polarization has been previously observed in cool M-dwarf stars (Miles-Páez et al. 2015) in optical wavelengths. However, the origin of those polarization signals is still unclear: they can be due to the strong magnetic field of the cool dwarf, the presence of a dusty disk around the star, or the presence of nonuniformly distributed dust grains in the stellar photosphere. De Kok et al. (2011) also found time-variable polarization signals from a brown dwarf model with a dusty hot spot in its atmosphere. We also simulate polarization signals for more equator-on inclinations  $\sim 20^\circ$  and  $\sim 0^\circ$  (equator-on). The modeled time-averaged signal is  $\sim 0.04\%$  and  $\sim 0.07\%$ , respectively, for the two inclinations. Both of these signals are much higher than the measured value. This indicates that the inclination of Luhman 16 A is very close to  $28^\circ$  if our GCM represents its atmosphere correctly. We discuss this further in Section 4.

The disk-integrated polarization signal is also anticorrelated to the disk-integrated flux from the object. This is because scattering from cloud particles are primarily responsible for the polarized flux in infrared wavelengths, and hence a higher disk-integrated flux hints at lower cloud coverage at that time instant and can give rise to a lower disk-integrated signal.

The angle of linear polarization also varies significantly for Luhman 16 A as shown in the bottom left panel of Figure 4. The angle of polarization varies between  $-7^\circ$  and  $8^\circ$  within one full rotational period. This kind of rotation of the plane of the polarization vector was also seen in models of brown dwarfs with a single dusty hot spot in de Kok et al. (2011). Our simulations suggest that the angle of polarization must show significant time variations if it arises from such circulation

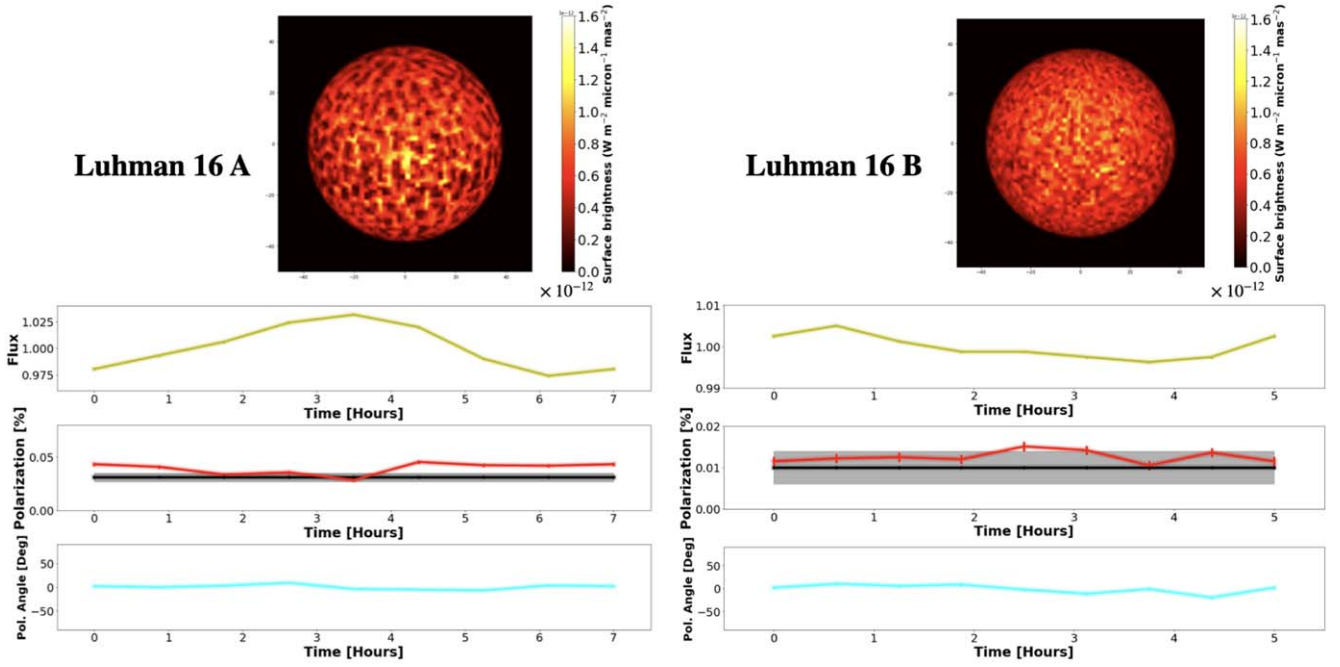


**Figure 4.** The left panel shows the radiative transfer result for Luhman 16 A. The top left panel shows the surface brightness map for the object. The second panel on the left shows the variability of thermal flux at  $1.6 \mu\text{m}$  with time as the object rotates with a period of 7 hr. The third left panel shows the linear polarization percentage vs. time with the solid red line. The solid black line and the shaded region show the measured polarization for the object. The bottom left panel shows the variation of the angle of polarization of the object with time using a cyan line. The same plots for Luhman 16 B (5 hr period) are shown in the right panels. Main point: Our models match the degree of linear polarization well for both objects but do not reproduce the observed optical variability amplitude of Luhman 16 B.

patterns. These polarization observations integrate over time-scales of several hours, which are comparable to the rotational period of these objects. We sum up the disk-integrated Stokes parameters from each of our time steps to calculate the disk-integrated degree of linear polarization and the angle of the polarization vector when it is time-integrated over one rotational period. We find that the time-integrated degree of linear polarization is 0.038% and the angle of linear polarization is  $-0^\circ.28$ . As has been outlined in Millar-Blanchaer et al. (2020) and Stolker et al. (2017), the polarization vector aligns itself with the spin axis if the disk-integrated polarization is dominated by equatorial bands of clouds and if oblateness dominates the polarization signal then the polarization vector is perpendicular to the spin axis. For Luhman 16 A, the polarization vector in all time steps as well as the disk-integrated polarization is aligned very closely to the spin axis, which suggests that our modeled polarization is mainly dominated by the equatorial bands of clouds in the GCM. The measured angle of linear polarization for Luhman 16 A by Millar-Blanchaer et al. (2020) is  $-32^\circ \pm 4^\circ$  relative to the north direction on the sky. This angle is not comparable to our model results since the on-sky orientation of the spin axis is unknown.

We check the sensitivity of the disk-integrated polarized signal to the typical cloud particle sizes of our GCMs. For Luhman 16 A, the typical cloud particle sizes are  $\sim 1 \mu\text{m}$  (we assume a gamma distribution of cloud particles) but we also simulate instances when the typical cloud particle sizes are  $\sim 10 \mu\text{m}$  and  $\sim 0.5 \mu\text{m}$ . Although changing the cloud particle sizes should also alter the circulation pattern in principle due to the dependence of cloud opacities on particle sizes, we neglect that subtlety here. Figure 5 shows the dependence of the disk-integrated polarization signal for both of our Luhman 16 A (top panels) and Luhman 16 B (bottom panels) models. The top left

panel shows the surface brightness map of the Luhman 16 A model when the typical cloud particle sizes are  $\sim 1 \mu\text{m}$  and the polarization percentage matches the observed polarization well. But when the particle sizes are increased to  $\sim 10 \mu\text{m}$  the surface brightness increases but the polarization signal declines by  $\sim 10$  times. The polarization signal increases slightly when the cloud particle sizes are taken to be  $\sim 0.5 \mu\text{m}$ . This indicates that the typical cloud particle sizes for Luhman 16 A, if the circulation patterns are representative of the reality, lie at  $\sim 0.5$ – $1 \mu\text{m}$ .

### 3.2. Luhman 16 B

The simulated surface brightness map of Luhman 16 B from the GCMs described in Section 2.1 is shown in Figure 4, top right panel. We assume an inclination of  $26^\circ$  for Luhman 16 B motivated by the results presented in Millar-Blanchaer et al. (2020). The time variability of thermal flux, the degree of linear polarization, and the angle of linear polarization are shown in the three other panels on the right from top to bottom. The modeled peak-to-peak variability for Luhman 16 B is  $\sim 1\%$ , which is much lower than the observed Luhman 16 B typical  $H$ -band variability amplitude of about 13% measured by Biller et al. (2013). This shows that our GCM is inadequate for explaining the variability of Luhman 16 B. This might happen due to the presence of a large cloud/cloudless feature on the globe of Luhman 16 B, which is not present in our GCM run.

The variability of the disk-integrated polarization signal for the Luhman 16 B model matches well the measured polarization of  $0.010\% \pm 0.004\%$  (Millar-Blanchaer et al. 2020) for an assumed inclination of  $26^\circ$  for the object. We explore the equator-on configuration for the Luhman 16 B model and find a disk-integrated polarization percentage of  $\sim 0.03\%$ , which is  $\sim 3$  times larger than the measured value. So, our model prefers an inclination of  $26^\circ$  for Luhman 16 B in



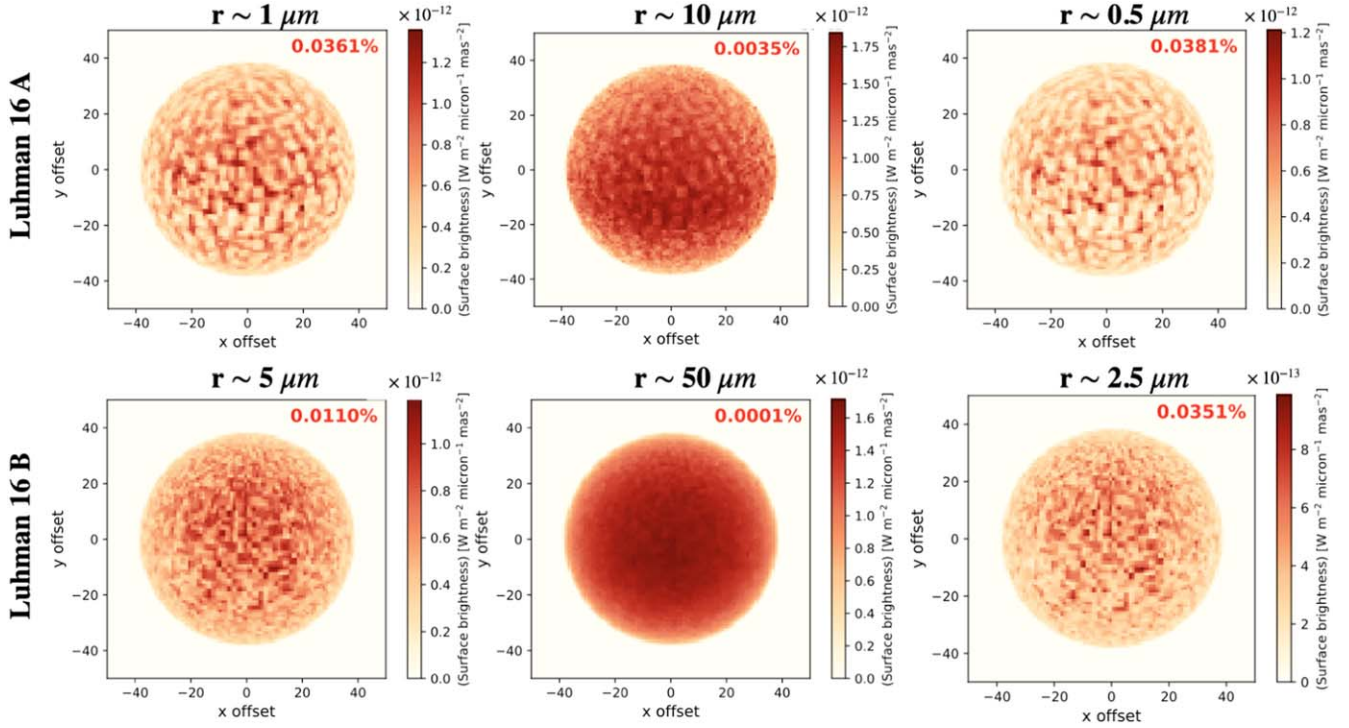


**Figure 5.** The top left, middle, and right panels show the surface brightness map for Luhman 16 A if the typical cloud particle sizes are  $1\ \mu\text{m}$  (original GCM),  $10\ \mu\text{m}$ , and  $0.5\ \mu\text{m}$ . The disk-integrated polarization for each case is shown on the top right of each plot window. The bottom left, middle, and right panels show the surface brightness map for Luhman 16 B if the typical cloud particle sizes are  $5\ \mu\text{m}$  (original GCM),  $50\ \mu\text{m}$ , and  $2.5\ \mu\text{m}$ . Please note that the color scheme is inverted. Main point: Luhman 16 A should have typical cloud particle sizes between  $0.5$  and  $1\ \mu\text{m}$  whereas Luhman 16 B should have cloud particle sizes of about  $5\ \mu\text{m}$ .

contrast to the much more equator-on configuration suggested by the variability analysis in Apai et al. (2021). However, we take this opportunity to reiterate that the detection significance of the measurement is only  $2.5\sigma$ .

The typical cloud particle sizes for the Luhman 16 B GCM are  $\sim 5\ \mu\text{m}$ . The disk-integrated polarization signals at  $1.6\ \mu\text{m}$  for cloud particle sizes of  $\sim 2.5\ \mu\text{m}$  and  $\sim 50\ \mu\text{m}$  are found to be  $0.0351\%$  and  $0.0001\%$ , respectively. The calculated signal with particles of  $\sim 50\ \mu\text{m}$  sizes is  $\sim 10$  times lower than the measured signal whereas the signal with typically  $\sim 2.5\ \mu\text{m}$  cloud particles is  $\sim 3$  times higher than the measurement. This is shown in Figure 5, lower panels. This suggests that the typical cloud particle sizes for Luhman 16 B are  $\sim 5\ \mu\text{m}$ .

The angle of linear polarization also varies significantly for Luhman 16 B between  $10^\circ$  and  $-20^\circ$ . This suggests that our polarization calculations for Luhman 16 B are dominated by the equatorial band of clouds in our Luhman 16 B circulation model. We find the time-averaged degree of linear polarization from our Luhman 16 B model is  $0.011\%$  by integrating the calculated signal over one rotation period of the object. This is in good agreement with the measured  $H$ -band polarization of  $0.01\% \pm 0.004\%$  for Luhman 16 B. This time-integrated polarization vector projects an angle of  $-1.56^\circ$  from the spin axis of the object. The measured time-averaged angle of the polarization vector is  $73^\circ$  (Millar-Blanchaer et al. 2020) relative to the north direction in the sky and hence is not directly comparable to our modeled angles since the on-sky orientation of the spin axis is unknown.

### 3.3. Modeling of Polarization Signal with Band Models

Single- and multiple-band models have often been used to model polarization signals from objects with nonuniformity in

cloud coverage (Millar-Blanchaer et al. 2020; Stolker et al. 2017). These have been motivated by observed band-like cloud patterns in Jupiter. Here, we try to explore if such models are adequate for calculations of disk-integrated polarization signals from objects like those modeled by our GCM runs or if we need circulation models like the one used in this work for interpreting future polarization observations from nonuniformly cloudy objects. We first assume that the real nature of circulation on a brown dwarf/exoplanet is represented by our circulation models. We then create models with multiple bands of clouds (“band models”) and test if they can reproduce the same polarization signal as we calculate from our GCM runs for Luhman 16 A and B. We assume that the cloud structure of our band models for Luhman 16 A and B is the same longitudinally averaged cloud structure shown in Figure 2. From the equator to the pole, each of the cloud profiles shown in Figure 2 (left panel) for Luhman 16 A forms a band with a latitude span of  $20^\circ$  in our band model for Luhman 16 A. Similarly, we construct our band model for Luhman 16 B with the averaged cloud profiles shown in Figure 2 (right panel) forming bands with latitude spans of  $20^\circ$ . The gas opacities used for radiative transfer for the GCM are also used for the band models of the corresponding objects to ensure similarities in all conditions between the GCMs and the band models except for the detailed circulation patterns dominating smaller length scales than the global jets. We compute the polarization signal from the band models for Luhman 16 A and Luhman 16 B using the same oblateness and inclinations used for the computations reported in Sections 3.1 and 3.2.

In Figure 6 the left panel shows the surface brightness map of the multiple-band model for Luhman 16 A and the right panel shows the same for the multiple-band model of Luhman 16 B. The disk-integrated polarization signal from this band

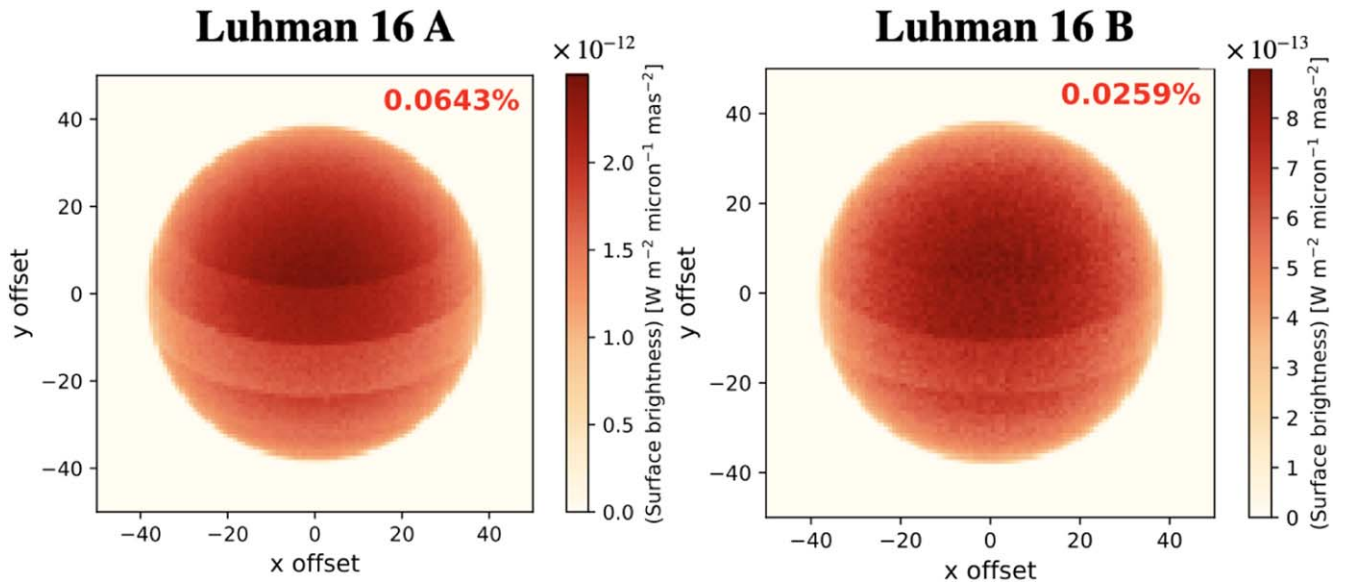


**Figure 6.** The left panel shows the surface brightness map of the simple band model for Luhman 16 A along with the  $1.6 \mu\text{m}$  disk-integrated polarization percentage denoted at the top in red. The right panel shows the same for the band model of Luhman 16 B. Please note that the color scheme is inverted. Main point: Band models tend to overestimate polarization signals.

model for Luhman 16 A is found to be 0.0643%. This is almost twice the signal calculated from the GCM for Luhman 16 A, where the polarization is found to be  $\sim 0.038\%$ . For Luhman 16 B, the calculated polarization from the band model is 0.0259% in contrast to the circulation model polarization percentage of  $\sim 0.011\%$ . The linear polarization vectors from the band models of both objects are aligned along the spin axis as has also been found from the GCMs. So in both cases the band models overestimate the disk-integrated polarization as compared with the GCMs even if other properties like inclination, oblateness, cloud optical properties, gas opacities, and the thermal structure are almost alike between the band and circulation models. This hints at the significant influence of smaller-scale vortices across the globe of these objects, which are present only in the circulation models, on the disk-integrated polarizations. Even if both the Luhman 16 A and B circulation models have a central equatorial band of clouds, a band model with single or multiple cloud bands might still overestimate the polarization signal from the object. These smaller-scale vortices of cloudy and cloud-free regions tend to decrease the overall disk-integrated polarization signal.

#### 4. Discussion

We first discuss some of the caveats, implications, and possibilities of future follow-up of our work and then summarize our findings in Section 5.

##### 4.1. GCM Parameter Choices

Our circulation models use the computational framework described in Tan & Showman (2021b), which necessarily involves some simplifications. For example, the GCMs and our subsequent radiative transfer calculations only consider the condensation of one cloud species (enstatite), which is an important cloud species in the temperature regime of our interest. Other cloud species like Fe and olivine are also suggested to be important sources of cloud opacity, and can alter the cloud radiative feedback, or cloud optical properties, of the object. The choice of condensation species itself is not

very critical as long as the cloud optical depths exceed the gaseous optical depths (Tan & Showman 2021a). However, different cloud species like Fe might follow a different particle size distribution, which can have an effect on polarization signal calculations.

For our models presented here, we use a particular time snapshot of the circulation structure of these objects after they reach a quasi-steady state. However, these circulation patterns may continue to evolve further in time and therefore investigation of the long-term photometric and polarization variability may prove fruitful as well.

The circulation models used here can be sensitive to other assumptions as well, such as the drag strength deep in the brown dwarf atmosphere. The GCMs presented here have been calculated in the “strong drag” regime but this drag strength is highly uncertain as the interaction between the deeper interior and the atmosphere has not been properly characterized to date (Tan & Showman 2021a). This work uses these GCM runs for post-processing with the comprehensive radiative transfer tool ARTES, which allows us to make direct comparisons with observations, but there remains ample scope for further exploration of the parameter space of the circulation models themselves. In future work, we will explore a wider range of GCM parameter space for Luhman 16 A and B, and generic brown dwarfs, to examine the sensitivity of our radiative transfer results to the assumptions outlined above. The combination of GCM outputs and post-processing for the calculation of polarization and spectra appears to be a powerful tool.

##### 4.2. Spherical Cloud Particles

We assume cloud particles to be spherical throughout this study for simplicity, as is typical in the field, and use Mie particle scattering theory for the calculation of cloud scattering properties. However, nonspherical particles can have significantly different scattering phase functions especially at back-scattering angles as has been investigated in detail by Mishchenko et al. (1997). However, they showed that the

difference in cloud optical properties like the optical depth, single-scattering albedo, and asymmetry parameter between nonspherical and projected-area equivalent spherical distributions of particles is at maximum  $\sim 10\%$ . This suggests that considering nonspherical particles in our GCM will not significantly alter the cloud radiative forcing compared to the spherical particles assumed in this work.

Since the phase functions at backscattering angles differ significantly between spherical and nonspherical distributions of particles (Mishchenko et al. 1997), they can affect the disk-integrated polarization signals calculated in this work. This has also been shown in Stolker et al. (2017), where the departure from spherical particles has been treated with a “distribution of hollow spheres” approach (Min et al. 2005). We use a spherical cloud particle shape assumption to avoid additional complexity at this time, in our already complex modeling. We defer treating nonspherical cloud particles to future work as more polarimetric observations are obtained in the near future.

Lastly, optical constants for mineral aerosol particles can themselves be temperature dependent (Zeidler et al. 2015), which we ignore here. Neither the infrared emission spectra nor the polarimetric measurements of brown dwarfs are constrained enough at this point to investigate these effects.

#### 4.3. Improvements to Radiative Transfer and Opacities

All our calculations are done at a single wavelength of  $1.6\ \mu\text{m}$  whereas the polarimetric measurements with which we compare our models are often done in broader photometric wavelength bands (the  $H$  band for Luhman 16 A and Luhman 16 B). In this work, we do not perform radiative transfer calculations for multiple wavelengths within the photometric wavelength band of observations in making our comparison with data in order to avoid the much longer computational time required. But integrating the disk-integrated polarization across a photometric band might change the predicted polarization signal from GCMs especially if there are sharp molecular absorption or emission windows within the photometric band in question.

In future modeling work over a broader wavelength range, to fit both emission spectroscopy and polarization, additional computational efforts should be put into opacity variations around the globe. Gaseous opacities depend on both the local temperature and pressure, and recall here that we use the gaseous opacities for the globally averaged  $T$ - $P$  profile for our radiative transfer. We make this approximation because our main focus in this work is the calculation of the polarization signal and gas molecules are not important scattering sources in infrared wavelengths. The only way they affect the resultant infrared thermal polarized flux is with their absorption opacity. As the maximum fluctuation in temperature across the globe at a certain pressure level for Luhman 16 A is  $\sim 200\ \text{K}$  and that for Luhman 16 B is  $\sim 20\ \text{K}$ , the temperature dependence of gas opacity across the globe will be a weak effect and will not affect the net disk-integrated polarization signal significantly, but may become important in future work.

### 5. Conclusions

We have coupled pioneering 3D GCM calculations for brown dwarfs Luhman 16 A and B with the vector Monte Carlo radiative transfer code ARTES, in order to calculate the polarization signal in 3D. We summarize our findings in the

form of answers to the specific questions we promised to answer/explore in Section 1 here.

1. We find that GCMs, with nearly global enstatite clouds, can be used to explain the observed  $H$ -band disk-integrated degree of linear polarization from cloudy brown dwarfs Luhman 16 A and Luhman 16 B. We calculate the degree of linear polarization for Luhman 16 A to be  $0.038\%$  and the measured value is  $0.031\% \pm 0.004\%$ . For Luhman 16 B, our calculated degree of polarization is  $0.011\%$  and the measured polarization is  $0.010\% \pm 0.004\%$ .
2. The typical variability amplitude observed in Luhman 16 A is also reproduced from the thermal flux calculated from our GCM for Luhman 16 A. However, our Luhman 16 B GCM underestimates the variability amplitudes from observations of Luhman 16 B. However, in all cases the observed variability for Luhman 16 A is not at  $1.6\ \mu\text{m}$ , the wavelength we model here.
3. If our circulation patterns are representative of the circulation patterns on these objects, then we find that the preferred spin axis inclination for Luhman 16 A is  $\sim 28^\circ$  whereas that for Luhman 16 B is  $\sim 26^\circ$ . We find that the disk-integrated polarization signals calculated from GCMs also decline as one moves from equator-on to pole-on configurations.
4. We also find that decreasing cloud particle sizes generally increases the disk-integrated polarization signal. For our GCM to match the observations for Luhman 16 A, we find that the typical cloud particle sizes should be within  $0.5$ – $1\ \mu\text{m}$ . For Luhman 16 B, cloud particles should be around  $5\ \mu\text{m}$  as  $2.5\ \mu\text{m}$  and  $50\ \mu\text{m}$  overestimate and underestimate the disk-integrated polarization, respectively.
5. Simpler cloud band models with one or multiple bands have often been used to interpret polarization measurements from nonuniformly cloud-covered objects. We find that even if we use cloud profiles very similar to the GCMs keeping every other important parameter such as oblateness and inclination the same, these band models tend to overestimate the disk-integrated polarization signal as compared with the GCMs. This suggests that smaller-scale vortices tend to decrease the disk-integrated polarizations in brown dwarfs and are important factors influencing the polarized emission. This also indicates that if the real cloud circulation of any object is like the GCMs then band models might not be adequate for interpreting disk-integrated polarization measurements from them.

In our follow-up work we will expand to multiwavelength polarization predictions, for both Luhman 16 A and B, and for brown dwarfs generally over a larger parameter phase space, given the larger data sets being accumulated (Jensen-Clem et al. 2020; van Holstein et al. 2021). We will also explore a wider range of GCMs for Luhman 16 A and Luhman 16 B, to assess whether the observed broadband photometric variability in the visible and near-infrared, as well as the polarization signal, can be interpreted in the framework of one model. Also, our cloudy GCMs for Luhman 16 A and B do not reproduce the multiple band-like circulation patterns inferred by Apai et al. (2021) for Luhman 16 B from TESS observations. Further exploration of our GCM parameter space for these objects and



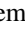




investigation of the circulation patterns and the disk-integrated polarization signals arising from them will significantly progress our understanding of brown dwarf clouds.

S.M. thanks the UC Regents Fellowship program for supporting him for this work. J.J.F. acknowledges support from the Simons Foundation. R.J.-C. acknowledges support from NSF AAG grant ATI2103241. We acknowledge use of the lux supercomputer at UC Santa Cruz, funded by NSF MRI grant AST 1828315. We thank Maxwell Millar-Blanchaer and the anonymous referee for valuable comments that helped to improve the paper. We also thank Tomas Stolker for help and guidance about the ARTES code and Xi Zhang for useful discussions.

*Software:* ARTES (Stolker et al. 2017), PICASO (Batalha et al. 2019), pandas (McKinney 2010), NumPy (van der Walt et al. 2011), IPython (Pérez & Granger 2007), Jupyter (Kluyver et al. 2016), matplotlib (Hunter 2007).

### ORCID iDs

Sagnick Mukherjee  <https://orcid.org/0000-0003-1622-1302>  
Jonathan J. Fortney  <https://orcid.org/0000-0002-9843-4354>  
Rebecca Jensen-Clem  <https://orcid.org/0000-0003-0054-2953>  
Xianyu Tan  <https://orcid.org/0000-0003-2278-6932>  
Mark S. Marley  <https://orcid.org/0000-0002-5251-2943>  
Natasha E. Batalha  <https://orcid.org/0000-0003-1240-6844>

### References

- Abel, M., Frommhold, L., Li, X., & Hunt, K. L. C. 2011, *JPCA*, **115**, 6805  
Ackerman, A. S., & Marley, M. S. 2001, *ApJ*, **556**, 872  
Apai, D., Nardiello, D., & Bedin, L. R. 2021, *ApJ*, **906**, 64  
Azzam, A. A. A., Tennyson, J., Yurchenko, S. N., & Naumenko, O. V. 2016, *MNRAS*, **460**, 4063  
Barber, R. J., Tennyson, J., Harris, G. J., & Tolchenov, R. N. 2006, *MNRAS*, **368**, 1087  
Batalha, N., Freedman, R., Lupu, R., & Marley, M. 2020, Resampled Opacity Database for PICASO v2, 1.0, Zenodo, doi:10.5281/zenodo.3759675  
Batalha, N. E., Marley, M. S., Lewis, N. K., & Fortney, J. J. 2019, *ApJ*, **878**, 70  
Beuzit, J. L., Vigan, A., Mouillet, D., et al. 2019, *A&A*, **631**, A155  
Biller, B. A., Crossfield, I. J. M., Mancini, L., et al. 2013, *ApJL*, **778**, L10  
Artigau, É., Bouchard, S., Doyon, R., & Lafrenière, D. 2009, *ApJ*, **701**, 1534  
Buenzli, E., Marley, M. S., Apai, D., et al. 2015, *ApJ*, **812**, 163  
Burgasser, A. J., Marley, M. S., Ackerman, A. S., et al. 2002, *ApJL*, **571**, L151  
Burgasser, A. J., Sheppard, S. S., & Luhman, K. L. 2013, *ApJ*, **772**, 129  
Crossfield, I. J. M., Biller, B., Schlieder, J. E., et al. 2014, *Natur*, **505**, 654  
de Kok, R. J., Stam, D. M., & Karalidi, T. 2011, *ApJ*, **741**, 59  
Eriksson, S. C., Janson, M., & Calissendorff, P. 2019, *A&A*, **629**, A145  
Girardin, F., Artigau, É., & Doyon, R. 2013, *ApJ*, **767**, 61  
Goldman, B., Pitann, J., Zapatero Osorio, M. R., et al. 2009, *A&A*, **502**, 929  
Hansen, J. E. 1971, *JATIS*, **28**, 1400  
Hansen, J. E., & Travis, L. D. 1974, *SSRv*, **16**, 527  
Helling, C., & Casewell, S. 2014, *A&ARv*, **22**, 80  
Huang, X., Gamache, R. R., Freedman, R. S., Schwenke, D. W., & Lee, T. J. 2014, *JQSRT*, **147**, 134  
Hunter, J. D. 2007, *CSE*, **9**, 90  
Jensen-Clem, R., Millar-Blanchaer, M., Mawet, D., et al. 2016, *ApJ*, **820**, 111  
Jensen-Clem, R., Millar-Blanchaer, M. A., van Holstein, R. G., et al. 2020, *AJ*, **160**, 286  
Kirkpatrick, J. D. 2005, *ARA&A*, **43**, 195  
Kluyver, T., Ragan-Kelley, B., Pérez, F., et al. 2016, in 20th Int. Conf. on Electronic Publishing (Amsterdam: IOS Press), 87  
Kniazev, A. Y., Vaisanen, P., Mužić, K., et al. 2013, *ApJ*, **770**, 124  
Li, G., Gordon, I. E., Rothman, L. S., et al. 2015, *ApJS*, **216**, 15  
Luhman, K. L. 2013, *ApJL*, **767**, L1  
Macintosh, B., Graham, J. R., Ingraham, P., et al. 2014, *PNAS*, **111**, 12661  
Manjavacas, E., Miles-Pérez, P. A., Zapatero-Osorio, M. R., et al. 2017, *MNRAS*, **468**, 3024  
Marley, M. S., & Robinson, T. D. 2015, *ARA&A*, **53**, 279  
Marley, M. S., & Sengupta, S. 2011, *MNRAS*, **417**, 2874  
McKemmish, L. K., Yurchenko, S. N., & Tennyson, J. 2016, *MNRAS*, **463**, 771  
McKinney, W. 2010, in Proc. 9th Python in Science Conf., ed. S. van der Walt & J. Millman (Austin, TX: SciPy), 51  
Ménard, F., Delfosse, X., & Monin, J. L. 2002, *A&A*, **396**, L35  
Miles-Pérez, P. A., Pallé, E., & Zapatero Osorio, M. R. 2017, *MNRAS*, **472**, 2297  
Miles-Pérez, P. A., Zapatero Osorio, M. R., & Pallé, E. 2015, *A&A*, **580**, L12  
Miles-Pérez, P. A., Zapatero Osorio, M. R., Pallé, E., & Peña Ramírez, K. 2013, *A&A*, **556**, A125  
Millar-Blanchaer, M. A., Girard, J. H., Karalidi, T., et al. 2020, *ApJ*, **894**, 42  
Millar-Blanchaer, M. A., Graham, J. R., Pueyo, L., et al. 2015, *ApJ*, **811**, 18  
Min, M., Hovenier, J. W., & de Koter, A. 2005, *A&A*, **432**, 909  
Mishchenko, M. I., Travis, L. D., Kahn, R. A., & West, R. A. 1997, *JGR*, **102**, 16831  
Pérez, F., & Granger, B. E. 2007, *CSE*, **9**, 21  
Radigan, J., Jayawardhana, R., Lafrenière, D., et al. 2012, *ApJ*, **750**, 105  
Radigan, J., Lafrenière, D., Jayawardhana, R., & Artigau, E. 2014, *ApJ*, **793**, 75  
Ryabchikova, T., Piskunov, N., Kurucz, R. L., et al. 2015, *PhyS*, **90**, 054005  
Sanghavi, S., & Shporer, A. 2018, *ApJ*, **866**, 28  
Sanghavi, S., & West, R. 2019, *ApJ*, **877**, 134  
Sanghavi, S., West, R., & Jiang, J. 2021, *ApJ*, **907**, 30  
Saumon, D., & Marley, M. S. 2008, *ApJ*, **689**, 1327  
Schwenke, D. W. 1998, *FaDi*, **109**, 321  
Scott, A., & Duley, W. W. 1996, *ApJS*, **105**, 401  
Sengupta, S., & Krishan, V. 2001, *ApJL*, **561**, L123  
Sengupta, S., & Marley, M. S. 2010, *ApJL*, **722**, L142  
Sengupta, S., & Marley, M. S. 2016, *ApJ*, **824**, 76  
Showman, A. P., Tan, X., & Parmentier, V. 2020, *SSRv*, **216**, 139  
Sousa-Silva, C., Al-Refaie, A. F., Tennyson, J., & Yurchenko, S. N. 2014, *MNRAS*, **446**, 2337  
Stolker, T., Min, M., Stam, D. M., et al. 2017, *A&A*, **607**, A42  
Tan, X., & Showman, A. P. 2019, *ApJ*, **874**, 111  
Tan, X., & Showman, A. P. 2021a, *MNRAS*, **502**, 2198  
Tan, X., & Showman, A. P. 2021b, *MNRAS*, **502**, 678  
Tata, R., Martín, E. L., Sengupta, S., et al. 2009, *A&A*, **508**, 1423  
Tennyson, J., & Yurchenko, S. 2018, *Atoms*, **6**, 26  
van der Walt, S., Colbert, S. C., & Varoquaux, G. 2011, *CSE*, **13**, 22  
van Holstein, R. G., Snik, F., Girard, J. H., et al. 2017, *Proc. SPIE*, **10400**, 1040015  
van Holstein, R. G., Stolker, T., Jensen-Clem, R., et al. 2021, *A&A*, **647**, A21  
Visscher, C., Lodders, K., Fegley, J. 2010, *ApJ*, **716**, 1060  
Vos, J. M., Biller, B. A., Bonavita, M., et al. 2019, *MNRAS*, **483**, 480  
Yurchenko, S. N., Barber, R. J., & Tennyson, J. 2011, *MNRAS*, **413**, 1828  
Yurchenko, S. N., & Tennyson, J. 2014, *MNRAS*, **440**, 1649  
Yurchenko, S. N., Tennyson, J., Barber, R. J., & Thiel, W. 2013, *JMoSp*, **291**, 69  
Zapatero Osorio, M. R., Béjar, V. J. S., Goldman, B., et al. 2011, *ApJ*, **740**, 4  
Zapatero Osorio, M. R., Caballero, J. A., & Béjar, V. J. S. 2005, *ApJ*, **621**, 445  
Zeidler, S., Mutschke, H., & Posch, T. 2015, *ApJ*, **798**, 125